

HouseCat6D - A Large-Scale Multi-Modal Category Level 6D Object Pose Dataset with Household Objects in Realistic Scenarios

HyunJun Jung^{*1}, Shun-Cheng Wu^{*1}, Patrick Ruhkamp^{*1}, Guangyao Zhai^{*1}, Hannah Schieber^{*2}, Giulia Rizzoli³, Pengyuan Wang¹, Hongcheng Zhao¹, Lorenzo Garattoni⁴, Sven Meier⁴, Daniel Roth², Nassir Navab¹, Benjamin Busam¹

¹ Technical University of Munich
³ University of Padova

² Friedrich-Alexander Universität (FAU) Erlangen-Nürnberg
⁴ Toyota Motor Europe * Equal Contribution

hyunjun.jung@tum.de

shuncheng.wu@tum.de

p.ruhkamp@tum.de

b.busam@tum.de

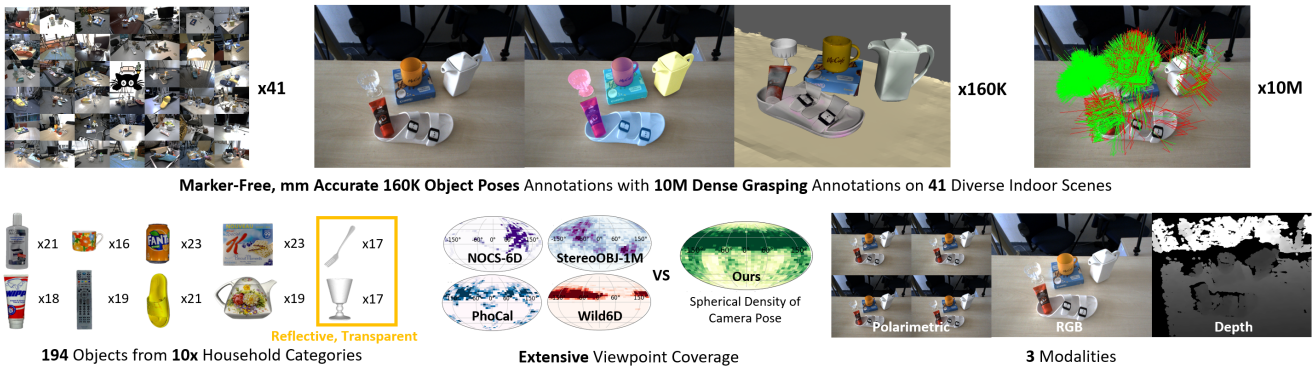


Figure 1. HouseCat6D is a multi-modal category level 6D object pose dataset with highly diverse household object categories of different photometric complexity and a high number of varying scenes covering large viewpoint distributions. It comprises room-scale high-quality camera trajectories and object poses without markers in realistic scenarios including occlusions as well as dense grasping pose annotation. Data includes synchronized RGB, depth from active stereo, and polarimetric RGB+P images in scenes comprising objects without texture, strong reflections, or translucency.

Abstract

Estimating the 6D pose of objects is a major 3D computer vision problem. Since the promising outcomes from instance-level approaches, research heads also move towards category-level pose estimation for more practical application scenarios. However, unlike well-established instance-level pose datasets, available category-level datasets lack annotation quality and provided pose quantity. We propose the new category-level 6D pose dataset **HouseCat6D** featuring **1) Multi-modality** of Polarimetric RGB and Depth (RGBD+P), **2) Highly diverse** 194 objects of 10 household object categories including 2 photometrically challenging categories, **3) High-quality** pose annotation with an error range of only 1.35 mm to 1.74 mm, **4) 41 large-scale** scenes with extensive viewpoint coverage and occlusions, **5) Checkerboard-free** envi-

ronment throughout the entire scene, and **6) Additionally** annotated dense 6D parallel-jaw grasps. Furthermore, we also provide benchmark results of state-of-the-art category-level pose estimation networks.

1. Introduction

6D pose estimation is one of the cornerstones in many computer vision tasks, especially for interactions like robotic grasping [54, 58, 59] or augmented reality [16]. Many methods have been proposed to solve this task from various perspectives and achieve outstanding results on public benchmarks [5, 21, 29, 56]. Most of the methods focus on instance-level where each network is trained and tested on a single object instance [36, 51]. However, generalization and applicability are limited, as the object mesh is required, and an individual network needs to be trained

Table 1. **Dataset Overview.** HouseCat6D represents a large-scale and highly accurate category-level 6D pose dataset that combines the advantages of various established datasets (e.g. extensive pose coverage, highly accurate GT, occlusions cases, and grasping annotation).

Dataset	RGB	Depth	Polarisation	Real	Multi-View	mm-accurate GT	Occlusion	Symmetry	Transparent	Reflective	Grasping	Pose Density	Pose Variation	Workspace	Categories	Objects	Scenes
FAT [47]	✓	✓			✓	✓	✓	✓							-	21	> 1k
BlenderProc [10]	✓	✓			✓	✓	✓	✓							-	-	> 1k
LabelFusion [40]	✓	✓		✓			✓	✓							-	12	138
Linemod [3, 21]	✓	✓					✓	✓							-	15	15
Toyota Light [23]	✓	✓		✓			✓	✓							-	21	21
YCB [5, 56]	✓	✓		✓			✓	✓							-	21	92
T-LESS [22]	✓	✓		✓			✓	✓							-	30	20
HomebrewedDB [29]	✓	✓		✓			✓	✓							-	33	13
ITODD [13]		✓		✓	✓	✓	✓	✓		(✓)					-	28	800
GraspNet-1Billion [17]	✓	✓		✓	✓		✓	✓			✓	+++	+++	+	-	88	190
HOPE [49]	✓	✓		✓	✓		✓	(✓)				++++	++++	+++	-	28	50
StereoOBJ-1M [33]	✓			✓	✓	✓	✓	✓	✓	✓		++++	++++	+++	-	18	183
kPAM [39]	✓	✓		✓			✓	✓							2	91	362
TOD [34]	✓	✓		✓	✓	✓	✓	✓	✓						3	20	10
Wild6D [18]	✓	✓		✓	✓		✓	✓	(✓)			++	++	++++	5	162	486
NOCS [52]	✓	✓		✓	✓		✓	✓				+	+	++	6	42	18
PhoCaL [53]	✓	✓	✓	✓	✓	✓	✓	✓	✓	✓		+++	+++	+	8	60	24
HouseCat6D (Ours)	✓	✓	✓	✓	✓	✓	✓	✓	✓	✓	✓	+++++	+++++	+++++	10	194	41

for each instance. Recent methods focus on category-level pose estimation [8, 32, 37, 38, 52] by training on multiple objects within one category. They can later generalize to unseen objects from the same category. However, a significant limitation blocking further progress is the lack of datasets for training and evaluation that fulfills all criteria like large-scale, accurate, and realistic. Existing category-level datasets only comply partly, e.g. high quantity and low quality [52], or high quality but insufficient quantity [53].

To this end, we propose a new category-level dataset HouseCat6D. It consists of high-quality ground-truth annotations on diverse objects acquired by multiple sensor modalities with extensive viewpoint coverage. Our dataset includes 194 objects from 10 different categories, including photometrically challenging classes such as glass and cutlery (Fig. 1), occlusion cases, and 3 sensor modalities, *i.e.* RGB, depth, and polarimetric images, with a total of 23.5k frames and approx. 160k annotated object poses. We additionally provide 10M grasp pose annotations to a subset of the dataset, endowing it with the capacity of serving robotic manipulation tasks, e.g., category-level robotic grasping [55]. Our dataset recording relies on an accurate external infrared tracking system and additional subsequent post-processing through sparse bundle adjustment to avoid errors induced by timestamp offsets and motion blur of the freely moving camera rig [43, 44]. Specifically, we conduct three calibrations, *i.e.* pivot calibration, timestamp calibration, and hand-eye-calibration. For the times-

tamp calibration, we adopt existing methods [14, 25] adjusted to our setup with an ICP-based refinement. For the hand-eye-calibration, we improve the calibration from recent work [53], by aggregating multiple measurements of a ChArUcO [2] calibration board (cf. Sec. 3.3). Compared to the recent PhoCaL dataset [53] that relies on a robotic end-effector to estimate poses and thus has limited viewpoint coverage and backgrounds, our method provides accurate object pose annotation and wide viewpoint coverage while providing pose annotations of similar quality. We use active stereo as depth maps which is more reliable on different surface materials [27, 53]. In addition to the typical RGB and depth, we provide polarimetric images with four different filter angles. Recent investigations have shown that this modality is especially suitable for tasks such as depth and surface normal estimation [28, 30, 50], and 6D pose estimation [19], especially for photometrically challenging objects or surfaces. In summary, our main contributions are:

1. We propose HouseCat6D¹ a **large-scale multi-modal category-level object pose dataset** with RGBD + RGBP data, comprising 194 high-quality 3D models of household objects including transparent and reflective objects in 41 scenes with broad viewpoint coverage, challenging occlusions and no markers.
2. We develop a novel **pipeline for annotation, recording, and accuracy-dependent post-processing** to

¹<https://github.com/Junggy/HouseCat6D>

achieve comparable accuracy to a robotic GT [53], but with a mobile handheld multi-camera rig. We detail all acquisition and calibration steps and make the **high-quality 6D object pose annotations together with 6D grasp labels** accessible to the community.

3. We provide and discuss the **benchmark evaluation results** on HouseCat6D for the SOTA category-level baselines CenterSnap [26], FS-Net [9], and GPV-Pose [11] for scientifically meaningful insights and to foster novel research in the field.

2. Related Work

The recent state-of-the-art methods are mostly data-driven approaches. A common need for these methods is a dataset for training and evaluation. In this section, we give an overview of existing datasets, and provide a summary of mentioned datasets in Tab. 1.

2.1. Instance-level 6D Object Pose Dataset

Early-stage datasets provide nontemporal consistent images. LineMOD [21] and LM-Occlusion [3] are arguably the most used datasets. They use an RGBD camera to annotate the pose of the objects. The camera pose is estimated with checkerboards, which constantly appear in all images. Although these two datasets were heavily used, the quality of object meshes and annotations varies [4]. Other datasets were proposed to overcome these issues. Such as HomebrewedDB [29] and others [12, 45]. However, those datasets still rely on checkerboard-based camera localization, or human-powered annotation [42], or a rotating table [13] to provide tolerable annotations. Consecutive datasets focus on providing sequential images with camera and object pose annotations. This allowed to investigate pose tracking approaches with temporal constraints [4, 20, 31]. One very popular such benchmark is YCB [56]. The annotation is achieved by leveraging an RGBD camera and Structure from Motion (SfM) [40]. Although this makes large-scale annotation possible, the annotation quality is bounded to the quality of the depth camera used [27, 53]. In comparison, the Laval 6DOF dataset [20] marker-based tracking results in high-quality annotations and checkerboard-free images. However, marker-induced depth artifacts need a depth map post-correction. On the other hand, StereoOBJ-1M [33] uses SfM with checkerboards in a more precise way to ensure quality and quantity. However, this also introduces checkerboards in every image. GraspNet-1Billion [17] provides parallel-jaw grasping labels besides object pose annotations, making it more feasible for downstream robotic bin-picking. However, the dataset has limited viewpoint changes and only simple backgrounds. In contrast, our dataset captures multiple household scenarios with adequate viewpoint coverage.

2.2. Category-level 6D Object Pose Dataset

Category-level pose estimation has been proposed to address generalizability in 6D pose estimation over multiple objects of the same category. The task is to generalize pose estimation per class and not for individual instances, which is challenging due to high intra-class variance. Many recent methods have been proposed [7, 9, 11, 26, 32, 37, 38, 46] to solve this problem due to its realistic setup. Only a few datasets exist which we will briefly review here.

The NOCS dataset [52] is the first category-level 6D pose dataset. It contains six categories and two sub-datasets, namely CAMERA25 and REAL275. In REAL275, the poses are aligned using checkerboards. For CAMERA25, ShapeNetCore [6] objects are placed in table-top scenarios. A dataset focusing more on the robotic field is kPam which uses keypoints. Manuelli *et al.* [39] capture kPam using a similar approach as [40]. They perform 3D reconstruction before manually labeling the keypoints on the 3D reconstruction. The dataset results in 117 training sequences and 245 testing sequences. While NOCS and kPAM contain solid objects, TOD [34] and PhoCaL [53] specifically focus on either translucent or transparent and reflective objects. TOD [34] is captured with a robotic arm and annotated keypoints and focuses on stereo images. Wang *et al.* [53] introduce a category-level dataset including polarimetric images besides RGBD only. For annotation, a robotic arm is used to tip individual objects with a calibrated pointer. Annotations are refined via ICP. Instead of using a robotic arm, Wild6D [18] is annotated via tracking. Every 50th keyframes is annotated and then registered via TEASER++ [57] and colored ICP [41]. The training dataset is label-free, and only the test dataset contains annotations. For recording, multiple iPhones are used to capture RGB images, depth, and point cloud. Fu *et al.* [18] introduce a Wild6D, an unlabeled RGBD video dataset with diverse scenes. They also investigate the use of additional synthetic labels and annotate a fraction of the real videos for evaluation. Other class-based datasets exist. Objectron [1] focuses on scale and provides over 14k scenes, however, only annotates 3D bounding boxes and does not give detailed shape information for the objects.

3. Dataset

Our dataset aims to provide large scale with large view coverage and high-quality pose annotation without a checkerboard. It is composed of 34 training scenes (20k frames), five test scenes (3k frames), and two validation scenes (1.4k frames). The scenes comprise objects from 10 household categories, including photometrically challenging objects like glass and cutlery with occlusions. With a total of 194 objects, each category contains 19 objects on average. Our dataset also features multiple modalities,

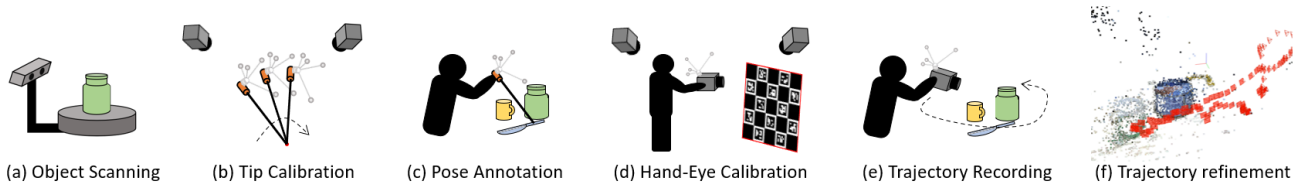


Figure 2. **Dataset Acquisition Pipeline.** (a): Pre-scanning 3D models. (b): Pivot calibration to calibrate measurement tip from the tracking body. (c): Pose annotation of objects using measurement tip. (d): Hand-Eye-Calibration to calibrate camera center of tracking body. (e): Camera trajectory recording (f): Post-processing step to reduce synchronization-induced trajectory error.

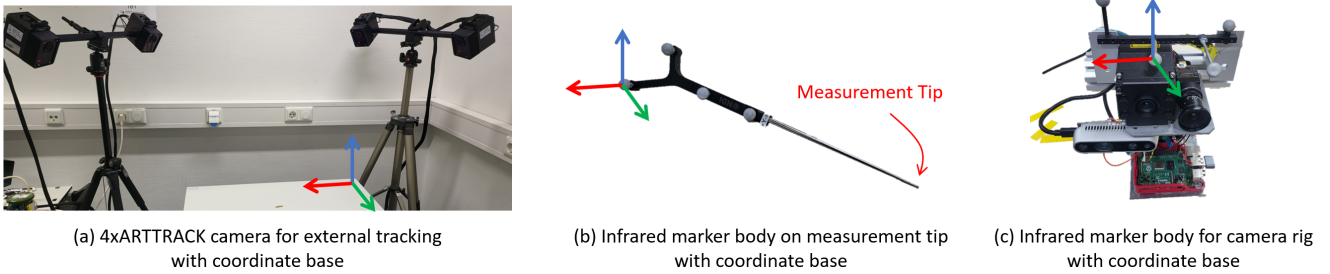


Figure 3. **Tracking System.** ARTTRACK2 tracking system and sets of infrared marker bodies we used for our setup. Once at least four infrared spheres are detected from at least two cameras, the tracking system provides the pose of the marker body as transformation from tracker system base to marker body base.

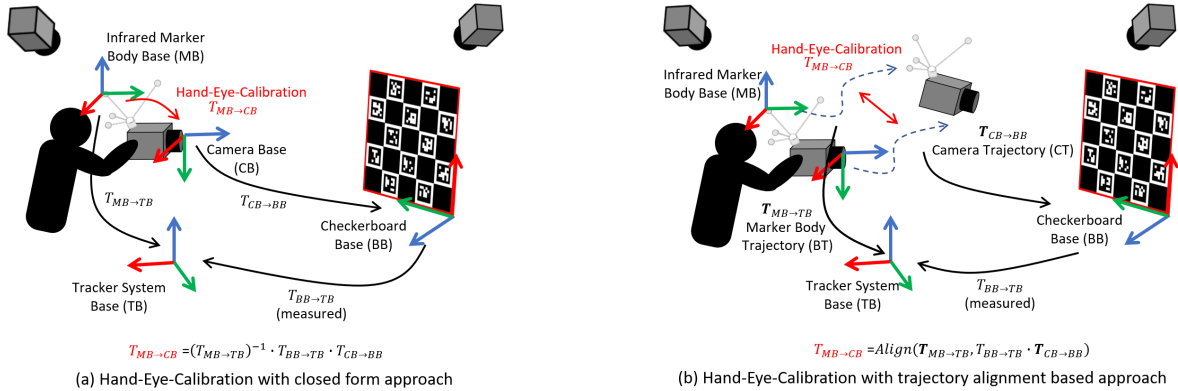


Figure 4. **Hand-Eye-Calibration.** Overview of two hand-eye-calibration methods which leverage the measured pose of the checkerboard. Although close form approach (a) produces good quality calibration, the quality of the calibration highly depends on the quality of the checkerboard detection and camera trajectory quality deviates when the camera pose deviates from the pose used for the calibration. Our newly proposed approach (b) takes more image captures into account. This makes it more robust against checkerboard detection errors in a wider range of camera poses.

namely RGB images, polarimetric images and depth maps. This section details our dataset. The acquisition setup is described in Fig. 2.

3.1. Objects & Hardware

Here, we briefly describe the hardware setup we use for the dataset acquisition. More detailed information, such as product names and their specs, is provided in the supplementary material. For our dataset, we choose 10 household categories to represent typical household scenarios:

bottle, box, can, cup, cutlery, glass, remote, shoe, teapot, and tube. All objects are scanned with a structured light stereo-based 3D scanner to ensure the quality of the reconstructed meshes. For the photometrically challenging categories, we use self-vanishing 3D scanning spray to enable scanning. For tracking the annotation tool and camera rig, we utilize an external tracker system composed of 4 infrared cameras to ensure tracking quality without using a checkerboard. Fig. 3 shows our camera setup and used tracking bodies for the annotation pipeline. We evaluate the accuracy

of the tracking with translation and rotational error [20] using a robotic setup (details in supplementary material). The average error is 0.67 mm / 0.12° in the static case and 0.92 mm / 0.16° in the dynamic tracking scenario. Our dataset comprises two main modalities: Polarimetric RGB image and active stereo depth. We use a dedicated sensor for each of the modalities. For polarimetric images, we use a polarimetric camera which produces four polarized RGB images for every shot. To measure depth, we decided on an active stereo depth sensor over Time-of-Flight sensors as active stereo depth provides, in general, more robust depth on photometrically challenging material [27]. To synchronize the two cameras, an external hardware trigger is used to trigger both cameras simultaneously.

3.2. Object Pose Annotation

Annotating the 6D pose of the object is, without a doubt, the most crucial part of a 6D pose dataset. In our dataset, we adopt the highly accurate object pose annotation pipeline from [53] by replacing the robotic end-effector pose with an IR tracking body. This ensures reliable tracking quality while covering a more extensive working volume. The annotation step follows tool tip calibration, 3D points measurement of the objects, and point correspondence with ICP-based refinement. In this subsection, we describe the details of each step.

Tip Calibration. The poses of the object meshes are annotated by measuring the 3D point using the tooltip. Thus, calibrating the location of the tip from the tracking body is essential to ensure the accuracy of the annotation. We use an NDI Active 4-Marker Planar Rigid Body (Northern Digital, Ontario Canada) as the measurement tip (Fig. 3 (b)). The tip is calibrated by fixing the tip while pivoting the tracking body and finding the optimal location of the point to minimize the variance of the fixed point (pivot calibration). The most common way to evaluate the quality of the pivot calibration is by measuring the variance of the fixed pivot point. We carefully calibrated with 18 points, with the final variance of the tip location of $\varepsilon = 0.040$ mm.

Pose Annotation. After the tip is calibrated from the tracking body, it can measure accurate 3D points in space in the world coordinates of the tracker system. We measure points for the initial point correspondence and ICP refinement as in [53] while covering around three times more points measurements with various surfaces of the object, thanks to the enlarged working space without the constraint given by using a robot arm [53]. We evaluate the quality of the pose annotation step by simulating the pose annotation pipeline on randomly selected three objects with the addition of pivot calibration error (Sec. 3.2) and static tracking

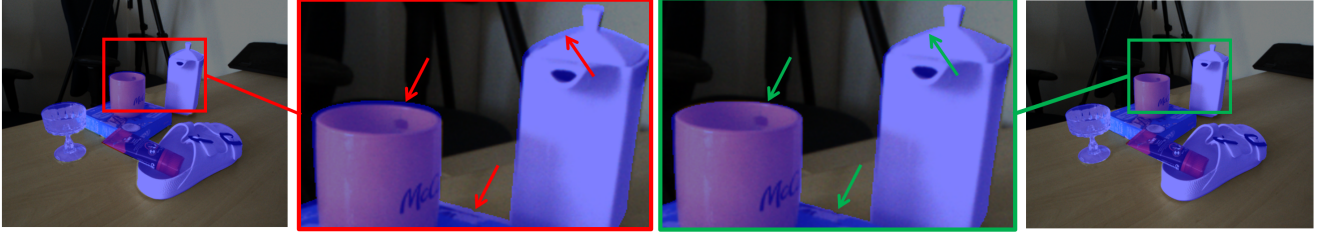
error (Sec. 3.1), which gives an average RMSE of 0.32 mm in translation and 0.43° in rotation.

3.3. Camera Trajectory Annotation

Another critical aspect of 6D pose dataset annotation is accurate camera trajectories. The object poses are annotated from the center of the tracker system, not from the center of the individual camera. Thus, the camera pose from the tracker system base has to be applied to obtain the 6D pose of the object from the camera center. In this section, we describe the detailed steps of camera trajectory annotation precisely.

Hand-Eye-Calibration In our scenario, Hand-Eye-Calibration obtains the transformation between the tracker marker body and the center of the camera image sensor. The most common way to perform Hand-Eye-Calibration [48] is detecting the checkerboard multiple times via camera while tracking the body of the camera from an external source and optimizing both checkerboard base from the tracker system base $T_{BB \rightarrow TB}$ and camera base from the marker body base $T_{MB \rightarrow CB}$ (hand-eye-calibration). The recent work [53] proposes a way to leverage the measurement tip to measure $T_{BB \rightarrow TB}$ to make the optimization process simpler (Fig. 4 (a)). However, we found that the accuracy of the closed-form solution is often unreliable. To solve this issue, we propose a new hand-eye calibration, which takes into account multiple image captures (Fig. 4 (b)). We capture multiple static images from different locations to form two trajectories - one from the camera and one from the tracking body and extract a fixed offset matrix by applying Horn’s alignment method [24], which is the hand-eye-calibration matrix. Once the calibration $T_{MB \rightarrow CB}$ is obtained, we align the two trajectories and compare the errors to the calibration accuracy. The RMSE for this calibration is measured as 0.27 mm for the translation and 0.42° for the rotation.

Camera to Tracker Time Synchronization Another important aspect of using the external IR tracking system is the timestamp calibration between the tracking system and the camera image acquisition time. It can cause severe offset on poses depending on the movement of the camera. A common practice to synchronize the timestamp difference is to measure the trajectory of the camera from two modalities, via image and tracking system, along with their timestamp, and maximize the similarity between the trajectories. This brings the best timestamp offset [14, 25]. In our case, we use ICP-based trajectory alignment to find the best timestamp offset instead of using a similarity measure. We empirically find it is more robust to noise and able to synchronize two trajectories with arbitrary frequency without any



(a) Rendered object mask on camera trajectory without COLMAP refinement step (b) Rendered object mask on camera trajectory with COLMAP refinement step

Figure 5. **Post-Processing via Bundle Adjustment.** Example of COLMAP [43, 44] refinement on selected frame with large camera displacement. Even though our timestamp synchronization step reduces the effect of motion induced pose offset, subtle errors still remain ((a), marked red). In comparison, the post processing step significantly reduces the given offset error ((b), marked green).

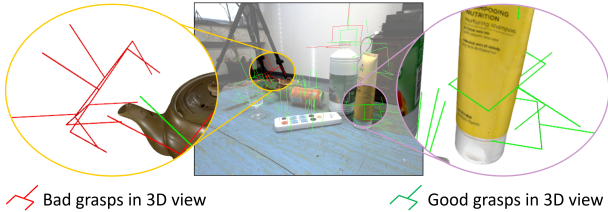


Figure 6. **Grasp Annotations.** After inspection of grasps, we annotate successful grasps (here coloured in green) and failed grasps (here red). We downsample the amount of annotated grasps for better visualization.

interpolation to match the frequency. For the camera timestamp, we use the hardware trigger timestamp. We evaluate the synchronization by simulating signals with measured noise. One with the tracking system error (Sec. 3.1) and one with detection-based error (Sec. 3.3). The simulated error is measured as 0.03 sec.

Pose Refinement Although the time synchronization improves the quality of the camera pose, the motion-induced pose error cannot be obliterated as the time synchronization is imperfect due to the noise in the checkerboard detection during the calibration [25] as well as the difference in individual camera image acquisition time due to its hardware condition. This effect can be observed when the camera motion involves large displacement between consecutive frames (Fig. 5, (a)). To tackle this issue, we use the RGB input to minimize the reprojection error with multi-view images. We use structure from motion [43, 44] with given initial poses and carefully selected fixed frames. The initial poses are used for initial feature matching and structure reconstruction. The fixed frames are excluded in the later bundle adjustment stage. These frames are manually picked upon careful inspection of the frame with the largest IoU between rendered object masks on the RGB image given the pose annotation. We show the improvement in Fig. 5, (b).

Table 2. **Accuracy Comparison against existing Datasets in mm.** RGBD-based datasets suffer from the standard deviation of the sensor [33]. Multi-view setups [33, 34] improve this. Our annotation quality is lower than robotic acquisition [53], however, we cover significantly more viewpoints and provide more accurate annotations than checkerboard-based datasets [33].

Dataset	RGBD based	TOD [34]	StereOBJ [33]	PhoCal [53]	Ours
3D Labeling	Depth Map	Multi-View	Multi-View	Robot	IR tracker
Point RMSE	≥ 17	3.4	2.3	0.80	$1.35 \leq \epsilon \leq 1.73$

3.4. Grasp Annotation

To facilitate downstream robotic manipulation tasks, e.g., robotic pick and place, we endow HouseCat6D with feasible 6D grasping poses for every object under each frame for a subset of collected sequences, following the well-established pipeline introduced in [15, 17]. Taking the annotation process for one object as an example: Firstly, we use antipodal sampling with an inspection of Isaac Gym [35] to distinguish the successful grasps \mathbf{G}_{obj}^s from failed ones \mathbf{G}_{obj}^{uns} to generate grasp candidates $\mathbf{G}_{obj} := \{\mathbf{G}_{obj}^s, \mathbf{G}_{obj}^{uns}\}$ for the object mesh. Then we use the obtained object pose under the tracker base $T_{obj \rightarrow TB}$ to transform \mathbf{G}_{obj} to the tracker frame where we also reconstruct and amend the background. Finally, we perform collision checking and prune grasping labels in the whole environment and reproject remaining grasps \mathbf{G}_{TB} to each camera frame in the whole sequence according to the transformation from the tracker base to each camera base $T_{TB \rightarrow CB}$. An annotated example is shown in Fig. 6. More details about the annotation pipeline and parameters can be found in the supplementary material.

3.5. Pose Annotation Quality Evaluation

For the evaluation of the annotation quality of object poses, we report the point-wise RMSE between objects and the camera center with and without the consideration of three systematic errors: tracking system error (Sec. 3.1), pose annotation error (Sec. 3.2) and hand-eye-calibration error (Sec. 3.3). As the accuracy gain from the structure-from-motion cannot be directly quantified, we report the RMSE with upper- and lower bounds. In the upper bound,

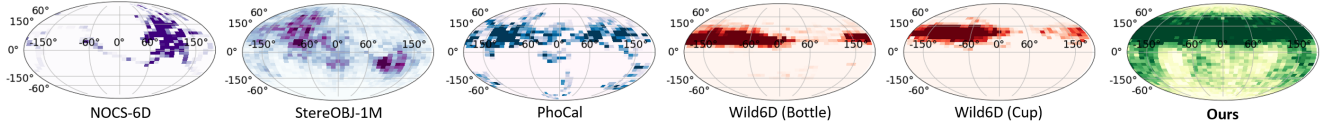


Figure 7. **Pose Distribution.** The pose distribution for category-level datasets NOCS [52] (Test), StereOBJ-1M [33] (Val), PhoCal [53] (Train), two categories of Wild6D [18] and Ours is plotted as the Mollweide projection of the spherical histogram, to exemplify the density and pose variation. Ours shows larger diversity of poses around objects, also for the lower hemisphere, and denser overall distribution.

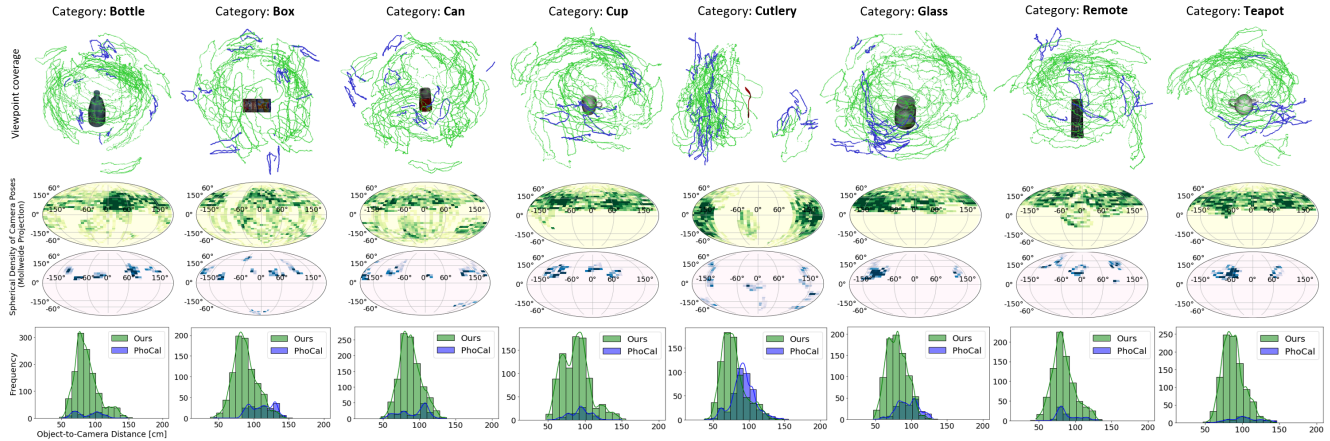


Figure 8. **Pose Distribution per Category.** We compare the pose distribution of HouseCat6D (green) against PhoCal [53] dataset (blue), for the categories included in both of them. The trajectory visualisation (top) verifies the much larger and better distributed pose coverage of our HouseCat6D dataset. Compared is further the rotational pose coverage as spherical histogram plotted as Mollweide projection (centre) and the object-to-camera distance as a histogram with relative frequency against the distance in cm (bottom).

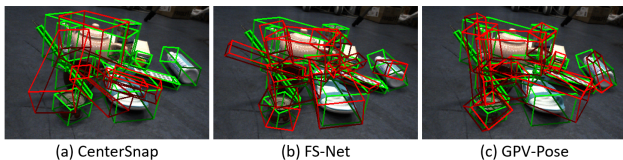


Figure 9. **Qualitative Baseline Comparisons.** Visualization of the baseline predictions on the test set of HouseCat6D for (a) CenterSnap [26], (b) FS-Net [9], and (c) GPV-Pose [11]. Predictions are red, ground truth is green.

we report the number with the object annotation error and the static tracking error, assuming no synchronization error. In the lower bound, we include all three mentioned systematic errors including dynamic tracking error as the tracking system error. We report our annotation quality compared to recent datasets in Tab. 2. Our method achieves a low RMSE of 1.35 mm to 1.73 mm.

3.6. Scene Statistics

HouseCat6D features 41 large-scale scenes with 194 objects in 10 categories with grasping labels for 16 scenes. It comprises 34 training scenes with 124 objects, 5 test scenes with 50 objects, and 2 validation scenes with 20 objects for

servicing the object pose estimation task. For the 34 training scenes, a total of 20k frames are recorded. Each training scene contains, on average, 6 objects of different categories. On the other hand, 5 test scenes and 2 validation scenes consist of 3k and 1.4k frames. They are composed of 10 unseen objects per scene with different categories. Compared to other category-level datasets, our dataset covers the most diverse number of instances and categories. For robotic grasping, we provide 14 training, 1 validation, and 1 test scene. Nonetheless, all 16 scenes can serve to train a real grasping pipeline, as the test would be performed in a real-world setup where success rate serves as the main grasping metric.

3.7. Viewpoint Coverage

Established datasets in 6D pose estimation lack well-distributed and dense camera pose coverage around the object. They usually focus on the upper hemisphere, even for large-scale dataset variants like StereOBJ-1M [33]. In contrast, HouseCat6D provides very dense and well-distributed poses (cf. Fig. 7). In terms of category level, we compare our trajectories for mutual classes against the recent PhoCal [53] dataset, which provides very accurate annotations, but is limited in the range of motion by the robotic arm used

Table 3. **Quantitative Comparisons.** Class-wise evaluation of 3D IoU (at 25%, 50%) for CenterSnap [26], FS-Net [9], and GPV-Pose [11] on the test split of HouseCat6D, and evaluation on best method on reduced training set simulating the PhoCal dataset [53] (*FS-Net [9]).

Approach	3D ₂₅ / 3D ₅₀	Bottle	Box	Can	Cup	Remote	Teapot	Cutlery	Glass	Tube	Shoe
CenterSnap [26]	11.1 / 0.5	14.5 / 3.2	6.1 / 0	18.7 / 0.9	14.2 / 0.2	6.6 / 0.0	17.4 / 0.0	0.3 / 0.0	21.4 / 0.4	8.9 / 0.0	2.9 / 0.0
GPV-Pose [11]	68.3 / 36.2	65.0 / 43.2	31.9 / 15.9	99.3 / 78.5	90.8 / 49.1	62.8 / 46.6	66.3 / 53.0	41.3 / 11.5	96.7 / 21.2	73.0 / 15.7	52.3 / 34.0
FS-Net [9]	69.4 / 37.0	64.0 / 42.7	29.4 / 12.7	99.6 / 75.1	92.3 / 54.1	62.6 / 45.3	69.1 / 54.2	43.5 / 10.6	97.2 / 28.2	72.2 / 14.9	58.2 / 38.2
*FS-Net [9]	56.9 / 16.8	63.3 / 37.0	33.6 / 6.7	99.9 / 63.3	68.2 / 6.3	49.0 / 22.4	51.1 / 19.6	24.6 / 0.5	90.9 / 9.7	75.7 / 5.2	37.8 / 17.2

for acquisition (cf. Fig. 8).

4. Benchmark and Experiments

Commonly used 6D pose estimation methods are based on RGB-D input. RGB provides information about the object itself (the class). However, categories can show a high intra-class variability. Thus, the RGB image is first used to identify the object, and the depth map is leveraged consecutively to learn more about the shape and object boundaries. GPV-Pose [11] first segments the object in the RGB image and then applies back-projection of the segmented depth map to the 3D space where it predicts the pose using geometry-guided point-wise voting. FS-Net [9] extracts the 3D point cloud from the depth image based on 2D RGB object detection. From this, latent features are extracted using a residual network, and object size and translation are estimated. For our experiment using FS-Net [9], we follow the implementation of Di *et al.* [11]. While FS-Net and GPV-Pose rely on bounding box predictions or semantic segmentation masks, CenterSnap [26] is free of bounding boxes or segmentation masks and predicts in a single-stage the 3D shape, 6D pose, and size of the objects in one network. CenterSnap relies also on RGB-D and treats each object instance individually as spatial centers, whereby each center represents the entire shape of an object, including its size and 6D pose.

4.1. Evaluation Pipeline & Results

Our dataset consists of 34 training, 2 validation, and 5 test sequences. For the baseline results, we report the results on the test split. We report the intersection over union (IoU) result with a threshold of 25% and 50% in Tab. 3 (for the evaluations with other metrics, *e.g.* rotation and translation error, please check the supplementary material). CenterSnap [26] results in poor mean average precision (mAP) of 11.1 for 3D IoU at 25%. On the other hand, geometry-guided approaches, such as GPV-Pose [11] and FS-Net [9], show significantly better performance. GPV-Pose gives 68.3% mAP and FS-Net achieves the best average results with an mAP of 69.4% for 3D IoU at 25%. We believe this is because these two methods first localize and detect each object instance and then estimate shape and pose consecutively. This approach assumes that one already has a good detection result before running the remaining pipeline. Both methods benefit from accurate 2D detection

supervision in HouseCat6D during training which helps to provide fine-granular object localization during their first stage. CentreSnap, in contrast, constitutes an efficient one-stage approach towards the problem which allows for real-time reconstruction. However, it localizes the objects with Gaussian kernels around their 2D centers. We believe that this less accurate 2D information, together with relatively poor sensor depth quality, cause CenterSnap results to be significantly inferior on the challenging and partly-occluded scenes of our dataset.

To verify the impact of having more viewpoint coverage and objects in the dataset, we train FS-Net [9] on our dataset, but with a similar data distribution as in PhoCal [53] in terms of the reduced number of scenes, trajectories and pose coverage. The last row of Tab. 3 shows the results from training on the reduced dataset. This ablation confirms our motivation for the need to provide an extensive 6D object pose dataset with comprehensive pose coverage. Objects with a certain degree of overall symmetry in shape (like Box, Can, or Glass) only suffer to a relatively small extent from the reduced pose coverage during training. In contrast, objects with a distinct non-symmetric feature, *e.g.* the handle of a cup or teapot, show a significant drop in accuracy, especially in the more constrained 3D IoU at 50%. We also run additional ablation studies such as training on the reduced set but with only less coverage or fewer objects independently to show which impacts more for category level pose estimation, as well as training with rendered GT depth from the 3D mesh to show the impact of depth quality on the training. These results can be found in the supplementary material.

Compared to the widely used NOCS [52] dataset, our data contains cluttered scenes which lead to occluded object parts and objects in close proximity to each other as illustrated in Fig. 9. Current category-level 6D pose estimation pipelines mostly consider cases without occlusion. This leaves room for improvement, as can be seen by this first evaluation. To provide more insights, we provide the occlusion ratio in each category per frame in the dataset and occlusion comparison compared to NOCS [52] dataset in the supplementary material.

5. Discussion and Conclusion

We have introduced HouseCat6D, a large-scale 6D pose dataset acquired with a multi-modal camera rig and an ex-

ternal tracking system. It provides highly accurate pose annotations. The setup solves issues of established datasets by providing realistic scenes without markers for which object poses are well distributed in realistic scenarios. Additionally, our approach allows to include photometrically challenging objects without texture and translucent material as well as accurate robotic grasping annotations. On the other hand, our dataset has a few drawbacks from the limitation of the tracking system. First, it requires a manual annotation that is labor-intensive and time-consuming. This makes scaling the magnitude of the dataset difficult. Second, our tracking system limits the scene recording to indoor scenes as the system does not work under strong sunlight. However, with the given quality and quantity of the dataset, HouseCat6D overcomes many previous shortcomings and fosters novel research and development in the field of categorical pose estimation. HouseCat6D, therefore, paves the way for pose applications in everyday household situations.

References

- [1] Adel Ahmadyan, Liangkai Zhang, Artsiom Ablavatski, Jianing Wei, and Matthias Grundmann. Objectron: A large scale dataset of object-centric videos in the wild with pose annotations. In *Proceedings of the IEEE/CVF conference on computer vision and pattern recognition*, pages 7822–7831, 2021. 3
- [2] Gwon Hwan An, Siyeong Lee, Min-Woo Seo, Kugjin Yun, Won-Sik Cheong, and Suk-Ju Kang. Charuco board-based omnidirectional camera calibration method. *Electronics*, 7(12):421, 2018. 2
- [3] Eric Brachmann, Alexander Krull, Frank Michel, Stefan Gumhold, Jamie Shotton, and Carsten Rother. Learning 6d object pose estimation using 3d object coordinates. In *Proceedings of the European Conference on Computer Vision*, pages 536–551. Springer, 2014. 2, 3
- [4] Benjamin Busam, Hyun Jun Jung, and Nassir Navab. I like to move it: 6d pose estimation as an action decision process. *arXiv preprint arXiv:2009.12678*, 2020. 3
- [5] Berk Calli, Aaron Walsman, Arjun Singh, Siddhartha Srinivasa, Pieter Abbeel, and Aaron M Dollar. Benchmarking in manipulation research: The ycb object and model set and benchmarking protocols. *arXiv preprint arXiv:1502.03143*, 2015. 1, 2
- [6] Angel X Chang, Thomas Funkhouser, Leonidas Guibas, Pat Hanrahan, Qixing Huang, Zimo Li, Silvio Savarese, Manolis Savva, Shuran Song, Hao Su, et al. Shapenet: An information-rich 3d model repository. *arXiv preprint arXiv:1512.03012*, 2015. 3
- [7] Dengsheng Chen, Jun Li, Zheng Wang, and Kai Xu. Learning canonical shape space for category-level 6d object pose and size estimation. In *Proceedings of the IEEE/CVF conference on computer vision and pattern recognition*, pages 11973–11982, 2020. 3
- [8] Wei Chen, Xi Jia, Hyung Jin Chang, Jinming Duan, Linlin Shen, and Ales Leonardis. Fs-net: Fast shape-based network for category-level 6d object pose estimation with decoupled rotation mechanism. In *Proceedings of the IEEE/CVF Conference on Computer Vision and Pattern Recognition*, pages 1581–1590, 2021. 2
- [9] Wei Chen, Xi Jia, Hyung Jin Chang, Jinming Duan, Linlin Shen, and Ales Leonardis. Fs-net: Fast shape-based network for category-level 6d object pose estimation with decoupled rotation mechanism. In *Proceedings of the IEEE/CVF Conference on Computer Vision and Pattern Recognition (CVPR)*, pages 1581–1590, June 2021. 3, 7, 8
- [10] Maximilian Denninger, Martin Sundermeyer, Dominik Winkelbauer, Dmitry Olefir, Tomas Hodan, Youssef Zidan, Mohamad Elbadrawy, Markus Knauer, Harinandan Katam, and Ahsan Lodhi. Blenderproc: Reducing the reality gap with photorealistic rendering. In *International Conference on Robotics: Science and Systems, RSS 2020*, 2020. 2
- [11] Yan Di, Ruida Zhang, Zhiqiang Lou, Fabian Manhardt, Xi-angyang Ji, Nassir Navab, and Federico Tombari. Gpv-pose: Category-level object pose estimation via geometry-guided point-wise voting. In *Proceedings of the IEEE/CVF Conference on Computer Vision and Pattern Recognition*, pages 6781–6791, 2022. 3, 7, 8
- [12] Andreas Dumanoglou, Rigas Kouskouridas, Sotiris Malasiotis, and Tae-Kyun Kim. Recovering 6d object pose and predicting next-best-view in the crowd. In *Proceedings of the IEEE Conference on Computer Vision and Pattern Recognition*, pages 3583–3592, 2016. 3
- [13] Bertram Drost, Markus Ulrich, Paul Bergmann, Philipp Hartinger, and Carsten Steger. Introducing mvtec itodd - a dataset for 3d object recognition in industry. In *Proceedings of the IEEE International Conference on Computer Vision Workshops*, Oct 2017. 2, 3
- [14] Ulrich Eck, Frieder Pankratz, Christian Sandor, Gudrun Klinker, and Hamid Laga. Precise haptic device co-location for visuo-haptic augmented reality. *IEEE Transactions on Visualization and Computer Graphics*, 0:15, 09 2015. 2, 5
- [15] Clemens Eppner, Arsalan Mousavian, and Dieter Fox. Acronym: A large-scale grasp dataset based on simulation. In *2021 IEEE International Conference on Robotics and Automation (ICRA)*, pages 6222–6227. IEEE, 2021. 6
- [16] Marco Esposito, Benjamin Busam, Christoph Hennesperger, Julia Rackerseder, Nassir Navab, and Benjamin Frisch. Multimodal us-gamma imaging using collaborative robotics for cancer staging biopsies. *International journal of computer assisted radiology and surgery*, 11(9):1561–1571, 2016. 1
- [17] Hao-Shu Fang, Chenxi Wang, Minghao Gou, and Cewu Lu. Graspnet-1billion: A large-scale benchmark for general object grasping. In *Proceedings of the IEEE/CVF conference on computer vision and pattern recognition*, pages 11444–11453, 2020. 2, 3, 6
- [18] Yang Fu and Xiaolong Wang. Category-level 6d object pose estimation in the wild: A semi-supervised learning approach and a new dataset. *arXiv:2206.15436*, 2022. 2, 3, 7
- [19] Daoyi Gao, Yitong Li, Patrick Ruhkamp, Iuliia Skobleva, Magdalena Wysock, HyunJun Jung, Pengyuan Wang, Arturo Guridi, and Benjamin Busam. Polarimetric pose prediction, 2021. 2
- [20] Mathieu Garon, Denis Laurendeau, and Jean-François Lalonde. A framework for evaluating 6-DOF object trackers. In *Proceedings of the European Conference on Computer Vision*, 2018. 3, 5
- [21] Stefan Hinterstoisser, Stefan Holzer, Cedric Cagniart, Slobodan Ilic, Kurt Konolige, Nassir Navab, and Vincent Lepetit. Multimodal templates for real-time detection of texture-less objects in heavily cluttered scenes. In *Proceedings of the IEEE International Conference on Computer Vision*, pages 858–865. IEEE, 2011. 1, 2, 3
- [22] Tomáš Hodan, Pavel Haluza, Štěpán Obdržálek, Jiri Matas, Manolis Lourakis, and Xenophon Zabulis. T-less: An rgb-d dataset for 6d pose estimation of texture-less objects. In *2017 IEEE Winter Conference on Applications of Computer Vision (WACV)*, pages 880–888. IEEE, 2017. 2
- [23] Tomas Hodan, Frank Michel, Eric Brachmann, Wadim Kehl, Anders GlentBuch, Dirk Kraft, Bertram Drost, Joel Vidal, Stephan Ihrke, Xenophon Zabulis, et al. Bop: Benchmark for 6d object pose estimation. In *Proceedings of the European conference on computer vision (ECCV)*, pages 19–34, 2018. 2
- [24] Berthold Horn, Hugh Hilden, and Shahriar Negahdaripour. Closed-form solution of absolute orientation using orthonor-

- mal matrices. *Journal of the Optical Society of America A*, 5:1127–1135, 07 1988. 5
- [25] Manuel Huber, Michael Schlegel, and Gudrun Klinker. Temporal calibration in multisensor tracking setups. In *2009 8th IEEE International Symposium on Mixed and Augmented Reality*, pages 195–196. IEEE, 2009. 2, 5, 6
- [26] Muhammad Zubair Irshad, Thomas Kollar, Michael Laskey, Kevin Stone, and Zsolt Kira. Centersnap: Single-shot multi-object 3d shape reconstruction and categorical 6d pose and size estimation. In *2022 International Conference on Robotics and Automation (ICRA)*, pages 10632–10640, 2022. 3, 7, 8
- [27] HyunJun Jung, Patrick Ruhkamp, Guangyao Zhai, Nikolas Brasch, Yitong Li, Yannick Verdie, Jifei Song, Yiren Zhou, Anil Armagan, Slobodan Ilic, Ales Leonardis, and Benjamin Busam. Is my depth ground-truth good enough? hammer – highly accurate multi-modal dataset for dense 3d scene regression, 2022. 2, 3, 5
- [28] Agastya Kalra, Vage Taamazyan, Supreeth Krishna Rao, Kartik Venkataraman, Ramesh Raskar, and Achuta Kadambi. Deep polarization cues for transparent object segmentation. In *Proceedings of the IEEE Conference on Computer Vision and Pattern Recognition*, pages 8602–8611, 2020. 2
- [29] Roman Kaskman, Sergey Zakharov, Ivan Shugurov, and Slobodan Ilic. Homebreweddb: Rgb-d dataset for 6d pose estimation of 3d objects. *Proceedings of the IEEE International Conference on Computer Vision Workshops*, 2019. 1, 2, 3
- [30] Chenyang Lei, Chenyang Qi, Jiaxin Xie, Na Fan, Vladlen Koltun, and Qifeng Chen. Shape from polarization for complex scenes in the wild, 2021. 2
- [31] Yi Li, Gu Wang, Xiangyang Ji, Yu Xiang, and Dieter Fox. DeepIM: Deep iterative matching for 6d pose estimation. *International Journal of Computer Vision*, 128(3):657–678, nov 2019. 3
- [32] Jiehong Lin, Zewei Wei, Zhihao Li, Songcen Xu, Kui Jia, and Yuanqing Li. Dualposenet: Category-level 6d object pose and size estimation using dual pose network with refined learning of pose consistency. In *Proceedings of the IEEE/CVF International Conference on Computer Vision*, pages 3560–3569, 2021. 2, 3
- [33] Xingyu Liu, Shun Iwase, and Kris M Kitani. Stereobj-1m: Large-scale stereo image dataset for 6d object pose estimation. In *Proceedings of the IEEE International Conference on Computer Vision*, pages 10870–10879, 2021. 2, 3, 6, 7
- [34] Xingyu Liu, Rico Jonschkowski, Anelia Angelova, and Kurt Konolige. Keypose: Multi-view 3d labeling and keypoint estimation for transparent objects. In *Proceedings of the IEEE Conference on Computer Vision and Pattern Recognition*, pages 11602–11610, 2020. 2, 3, 6
- [35] Viktor Makoviychuk, Lukasz Wawrzyniak, Yunrong Guo, Michelle Lu, Kier Storey, Miles Macklin, David Hoeller, Nikita Rudin, Arthur Allshire, Ankur Handa, and Gavriel State. Isaac gym: High performance gpu-based physics simulation for robot learning, 2021. 6
- [36] Fabian Manhardt, Diego Martin Arroyo, Christian Rupprecht, Benjamin Busam, Tolga Birdal, Nassir Navab, and Federico Tombari. Explaining the ambiguity of object detection and 6d pose from visual data. In *Proceedings of the IEEE/CVF International Conference on Computer Vision*, pages 6841–6850, 2019. 1
- [37] Fabian Manhardt, Manuel Nickel, Sven Meier, Luca Minciullo, and Nassir Navab. Cps: Class-level 6d pose and shape estimation from monocular images. *arXiv preprint arXiv:2003.05848*, 2020. 2, 3
- [38] Fabian Manhardt, Gu Wang, Benjamin Busam, Manuel Nickel, Sven Meier, Luca Minciullo, Xiangyang Ji, and Nassir Navab. Cps++: Improving class-level 6d pose and shape estimation from monocular images with self-supervised learning. *arXiv preprint arXiv:2003.05848*, 2020. 2, 3
- [39] Lucas Manuelli, Wei Gao, Peter Florence, and Russ Tedrake. kpam: Keypoint affordances for category-level robotic manipulation. In *The International Symposium of Robotics Research*, pages 132–157. Springer, 2019. 2, 3
- [40] Pat Marion, Peter R Florence, Lucas Manuelli, and Russ Tedrake. Label fusion: A pipeline for generating ground truth labels for real rgbd data of cluttered scenes. In *IEEE International Conference on Robotics and Automation*, pages 3235–3242. IEEE, 2018. 2, 3
- [41] Jaesik Park, Qian-Yi Zhou, and Vladlen Koltun. Colored point cloud registration revisited. In *Proceedings of the IEEE international conference on computer vision*, pages 143–152, 2017. 3
- [42] Colin Rennie, Rahul Shome, Kostas E Bekris, and Alberto F De Souza. A dataset for improved rgbd-based object detection and pose estimation for warehouse pick-and-place. *IEEE Robotics and Automation Letters*, 1(2):1179–1185, 2016. 3
- [43] Johannes Lutz Schönberger and Jan-Michael Frahm. Structure-from-motion revisited. In *Conference on Computer Vision and Pattern Recognition (CVPR)*, 2016. 2, 6
- [44] Johannes Lutz Schönberger, Enliang Zheng, Marc Pollefeys, and Jan-Michael Frahm. Pixelwise view selection for unstructured multi-view stereo. In *European Conference on Computer Vision (ECCV)*, 2016. 2, 6
- [45] Alykhan Tejani, Danhang Tang, Rigas Kouskouridas, and Tae-Kyun Kim. Latent-class hough forests for 3D object detection and pose estimation. In *Proceedings of the European Conference on Computer Vision*, pages 462–477. Springer, 2014. 3
- [46] Meng Tian, Marcelo H Ang, and Gim Hee Lee. Shape prior deformation for categorical 6d object pose and size estimation. In *European Conference on Computer Vision*, pages 530–546. Springer, 2020. 3
- [47] Jonathan Tremblay, Thang To, and Stan Birchfield. Falling things: A synthetic dataset for 3d object detection and pose estimation. In *Proceedings of the IEEE Conference on Computer Vision and Pattern Recognition Workshops*, pages 2038–2041, 2018. 2
- [48] Roger Y Tsai, Reimar K Lenz, et al. A new technique for fully autonomous and efficient 3 d robotics hand/eye calibration. *IEEE Transactions on robotics and automation*, 5(3):345–358, 1989. 5
- [49] Stephen Tyree, Jonathan Tremblay, Thang To, Jia Cheng, Terry Mosier, Jeffrey Smith, and Stan Birchfield. 6-dof pose estimation of household objects for robotic manipulation: An accessible dataset and benchmark. In *2022 IEEE/RSJ*

- International Conference on Intelligent Robots and Systems (IROS)*, pages 13081–13088. IEEE, 2022. [2](#)
- [50] Yannick Verdié, Jifei Song, Barnabé Mas, Benjamin Busam, Ales Leonardis, and Steven McDonagh. Cromo: Cross-modal learning for monocular depth estimation. In *Proceedings of the IEEE/CVF Conference on Computer Vision and Pattern Recognition*, pages 3937–3947, 2022. [2](#)
- [51] Gu Wang, Fabian Manhardt, Federico Tombari, and Xiangyang Ji. Gdr-net: Geometry-guided direct regression network for monocular 6d object pose estimation. In *Proceedings of the IEEE/CVF Conference on Computer Vision and Pattern Recognition*, pages 16611–16621, 2021. [1](#)
- [52] He Wang, Srinath Sridhar, Jingwei Huang, Julien Valentin, Shuran Song, and Leonidas J Guibas. Normalized object coordinate space for category-level 6d object pose and size estimation. In *Proceedings of the IEEE Conference on Computer Vision and Pattern Recognition*, pages 2642–2651, 2019. [2](#), [3](#), [7](#), [8](#)
- [53] Pengyuan Wang, HyunJun Jung, Yitong Li, Siyuan Shen, Rahul Parthasarathy Srikanth, Lorenzo Garattoni, Sven Meier, Nassir Navab, and Benjamin Busam. Phocal: A multi-modal dataset for category-level object pose estimation with photometrically challenging objects. In *CVPR*, 2022. [2](#), [3](#), [5](#), [6](#), [7](#), [8](#)
- [54] Pengyuan Wang, Fabian Manhardt, Luca Minciullo, Lorenzo Garattoni, Sven Meier, Nassir Navab, and Benjamin Busam. Demograsp: Few-shot learning for robotic grasping with human demonstration. In *2021 IEEE/RSJ International Conference on Intelligent Robots and Systems (IROS)*, pages 5733–5740. IEEE, 2021. [1](#)
- [55] Hongtao Wen, Jianhang Yan, Wanli Peng, and Yi Sun. Transgrasp: Grasp pose estimation of a category of objects by transferring grasps from only one labeled instance. In *Computer Vision—ECCV 2022: 17th European Conference, Tel Aviv, Israel, October 23–27, 2022, Proceedings, Part XXXIX*, pages 445–461. Springer, 2022. [2](#)
- [56] Yu Xiang, Tanner Schmidt, Venkatraman Narayanan, and Dieter . Posecnn: A convolutional neural network for 6d object pose estimation in cluttered scenes. *Robotics: Science and Systems*, 2018. [1](#), [2](#), [3](#)
- [57] Heng Yang, Jingnan Shi, and Luca Carlone. Teaser: Fast and certifiable point cloud registration. *IEEE Transactions on Robotics*, 37(2):314–333, 2020. [3](#)
- [58] Guanyao Zhai, Dianye Huang, Shun-Cheng Wu, HyunJun Jung, Yan Di, Fabian Manhardt, Federico Tombari, Nassir Navab, and Benjamin Busam. Monograspnet: 6-dof grasping with a single rgb image. In *IEEE International Conference on Robotics and Automation*. IEEE, 2023. [1](#)
- [59] Guanyao Zhai, Yu Zheng, Ziwei Xu, Xin Kong, Yong Liu, Benjamin Busam, Yi Ren, Nassir Navab, and Zhengyou Zhang. Da² dataset: Toward dexterity-aware dual-arm grasping. *IEEE Robotics and Automation Letters*, 7(4):8941–8948, 2022. [1](#)

Supplementary Material for HouseCat6D Dataset



Figure 1. **Object Meshes from Symmetric and Partially Symmetric Shape Categories.** Glass (a), bottle (b), can (c) and tube (d) categories are the categories with distinctive symmetry axis. We align the y axis to the axis of symmetry. If one surface is larger in area than another side, the x -axis is aligned in perpendicular direction to it. All the objects are rendered in the same scale to highlight the size variance among the same category.

1. Object Meshes and Orientation

The HouseCat6D dataset features 194 highly diverse objects from 10 household object categories with different textures, sizes, and shapes. In this section, we show the meshes of the objects in each category and the descriptions of their orientation.

Glass HouseCat6D aligns the symmetry axis with the y axis for the (partially) symmetric objects. Glass objects in our dataset are fully symmetric around y axis in accordance with [10] who also align y axis and symmetry axis. The x and z axes serve as any orthogonal axes around the y axis as exemplified in Fig. 1 (a).

Bottle Unlike the glass objects, bottle objects in our dataset are sometimes not fully symmetric (i.e. frontal surface is wider than the side) as in Fig. 1 (b). In this case, we define the x axis perpendicular to the surface of larger area.

Can Similar to the bottle objects, can objects in our dataset sometimes are not fully symmetric (i.e. some cans are more square and one side is wider than the other side)

as shown in Fig. 1 (c). Like the bottle objects, we define the x axis perpendicular to the wider side.

Tube Tube objects in our dataset are partially symmetric in shape, such that one side is round at the end while flat on the other side as shown in Fig. 1 (d). As in the can and bottle category, we define the x axis perpendicular to the wider side.

Teapot In general, teapots have the shape of one (partially) symmetric body with a handle and tip where the liquid comes out. In our dataset, we use the y axis for the direction of the symmetric body and x axis for the direction from the handle to the tip as shown in Fig. 2 (a).

Cup For the cup category, we only use cups with handles that have the shape of one symmetric body with a handle. Thus, similar to the Teapot category, we align the y axis to the direction of the symmetric body and x with the direction from the handle to the other side of the body as shown in Fig. 2 (b).



Figure 2. **Object Meshes from (Partially) Symmetric Objects With a Handle.** Teapot (a) and cup (b) are the categories with objects that include a (partially) symmetric body with handle. We align the y axis with the symmetry axis of the body and the x axis with the direction from handle to the the other side of the body. All the objects are rendered in the same scale to highlight the size variance among the same category.



Figure 3. **Object Meshes from Flat Shape Categories.** Shoe (a), remote (b) and cutlery (c) are the categories with long, flat and non-symmetric shape. We oriented such shapes in a way that the y axis points in the direction of the upper side and x in the direction of the front side. All the objects are rendered in the same scale to highlight the size variance among the same category.



Figure 4. **Object Meshes for Box category.** Unlike the other categories, the sides of the box are rather defined by their texture. To allow networks to generalize in this category, we orient the meshes by their side length. We set y,x,z as direction of first, second and third longest side. All the objects are rendered in the same scale to highlight the size variance among the same category.

Shoe Shoes, in general, have a long, flat and non-symmetric shape. For this category, we use only the right side of the slipper as illustrated in Fig. 3 (a). We oriented shoes such that their upper side points in the direction of the y axis and the front side points in the direction of the x axis.

Remote Remotes have relatively flat bodies with long and non-symmetric shapes, as shown in Fig. 3 (b). Similar to the shoe category, remotes are oriented such that their upper side points in the direction of the y axis, and the front side is oriented in the direction of the x axis.

Cutlery Although the texture of the reflective surface makes a clear distinction between the cutlery category to any other category, the shape itself shares similarity

with shoe and remote category. It is flat, long, and non-symmetric (Fig. 3 (c)). Thus, it shares the same orientation scheme, the upper side is aligned with the y axis and the front side points in x direction.

Box Unlike other categories, the sides of the box are defined by their texture. Even a human observer has to inspect the textures on multiple sides of a box to judge which side is the front or upper side *etc.* To make it easier for networks to generalize the orientation of boxes, we orient them by the length of the sides independent of their textures. We use y,x,z for the direction of the first, second, and third longest side as shown in Fig. 4.

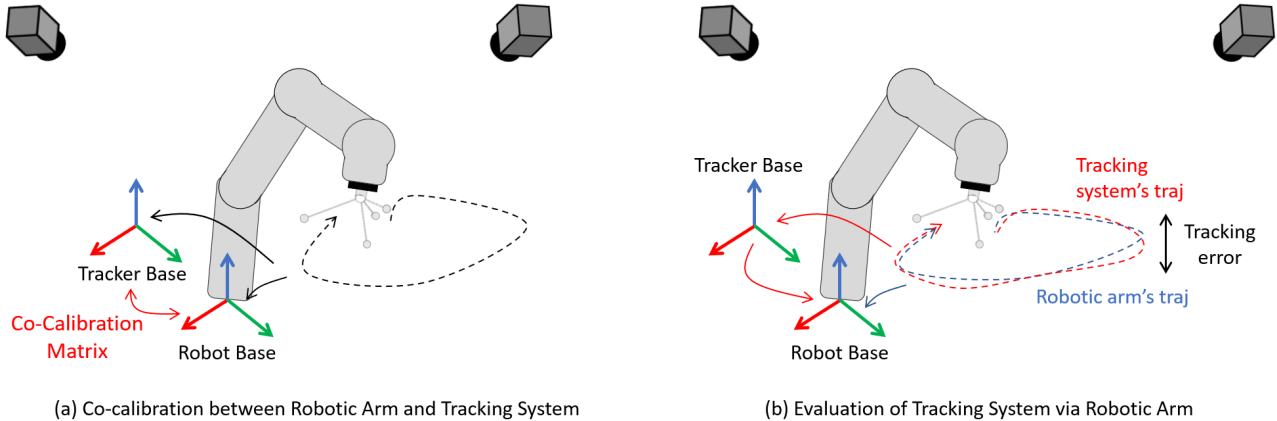


Figure 5. **Tracking System Evaluation.** We use a robotic arm to evaluate the quality of the tracking system. We first (a) co-calibrate the robot and the tracking system such that they share a common reference frame and then (b) run an example trajectory to calculate the difference between the trajectory obtained from the robot and the tracking system for error evaluation.

2. Hardware Details

In this section, we provide detailed information about hardware we used for the dataset acquisition.

3D Scanning As shown in Sec.1, our dataset comprises of 10 household categories such as bottle, box, can, cup, cutlery, glass, remote, shoe, teapot, tube. To ensure the high quality meshes we use 3D scanner equipped with turn table and structured light stereo system (EinScan-SP 3D Scanner, SHINING 3D Tech. Co., Ltd., Hangzhou, China), which produces single shot accuracy of ≤ 0.05 mm in a scanning volume of $1200 \times 1200 \times 1200$ mm³. For photometrically challenging categories like cutlery and glass, self-vanishing 3D scanning spray (AESUB Blue, Aesub, Recklinghausen, Germany) is applied prior to the scanning.

External Tracking System. To ensure broad viewpoint coverage with high-quality annotation without using a checkerboard, we utilize an external tracker system composed of 4 (2x Stereo) ARTTRACK2 cameras (Advanced Realtime Tracking GmbH & Co, Germany) with built-in infrared flash (NIR, 880 nm) and maximum tracking distance of 4.5 m for both object pose and camera pose annotation.

Cameras. Our multi-modal dataset comprises two main modalities: Polarimetric RGB image and active stereo depth. A Phoenix 5.0 MP Polarization camera with Sony IMX264MYR CMOS Polarsens (PHX050S1-QC, LUCID Vision Labs, Inc., Canada) sensor is used to produce the RGB+P images, and Intel RealSense D435 (RealSense D435i, Intel, USA) acquires the depth maps. We specifically choose D435 as the depth sensor over Time-of-Flight

sensors as active stereo depth provides, in general, more robust depth on photometrically challenging material [7]. To ensure the best synchronization between the two cameras, we use an external tracking signal provided by a Raspberry Pi (Raspberry Pi Foundation, United Kingdom) with GPIO output and later use the trigger signal as the timestamp of images for post-ex synchronization correction with the tracking system.

3. External Tracking System Evaluation

As mentioned in Sec. 3.2 in the main paper, we evaluate our IR-based external tracking system ARTTRACK2 via a robotic arm. We use a KUKA LBR iiwa 7 R800 (KUKA Roboter GmbH, Augsburg, Germany), a 7 DoF robotic arm certified for industrial use to provide ± 0.1 mm positional reproducibility, as the device to produce the ground truth pose for the comparison. In this section, we describe the detailed steps for the evaluation.

3.1. Robot-Tracker Co-Calibration

The first step to evaluate the tracking system with a robot is to co-calibrate the base of the robot and the tracking system. For this, we attach the calibrated IR tracking body on the robotic End-Effector (EE) as shown in Fig. 5 (a). We then acquire one trajectory from two different coordinate bases, one from the Robot base and the other one from the Tracker base. Similar to hand-eye calibration, we extract the static transformation between the two trajectories using the method of Horn [5]. In this case, the static transformation matrix is the transformation between Tracker Base and Robot Base (marked red in Fig. 5 (a)).

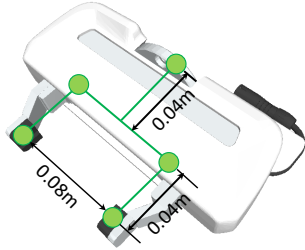


Figure 6. **The model of the parallel-jaw gripper**, whose finger depth is $0.04m$, maximum grasping width is $0.08m$, and the distance between the gripper base and the center of two fingers' base is $0.04m$.

3.2. Trajectory Error Evaluation

After co-calibration, we keep the tracking body on the robotic EE and make an evaluation trajectory that replicates the trajectory in one of the scenes. We repeat the trajectory twice, once with the robot stopping at every capturing position and once with the robot not stopping during the pose capture. The first trajectory serves as an evaluation for the tracking system accuracy in the static case, and the later trajectory serves as an evaluation in the dynamic case. As it is possible to obtain the pose of the tracking body from both, robot and tracking system, in the same coordinate frame using the co-calibration matrix, the error of the tracking system is calculated as the pose difference between the pose from the robotic arm and the pose from the tracking system (Fig. 5 (b)). We measure an error of $0.67\text{ mm} / 0.12^\circ$ in the static case and $0.92\text{ mm} / 0.16^\circ$ in the dynamic case.

4. Grasping Annotation Pipeline

In this section, we detail the grasping annotation process. The pipeline is illustrated in Fig. 7. For each scene, we first obtain the scene by reconstructing the background (e.g. table) with multiview depth and displacing the object meshes on the top of the background mesh according to their pose. After successfully reconstructing the scene, the meshes are sent to the antipodal sampling module to generate grasp candidates (Fig. 7.a). Then Isaac Gym [9] sorts out the good grasps among all candidates for each object by checking if grasping an object failed. Successful grasps are in green, while failed grasps are in red (Fig. 7.b). Then objects are projected to the tracker base along with their associated grasps to check the collisions and collided grasps are removed from the original ones. Finally, we project these checked grasps to each image base to obtain the ultimate dataset. (Fig. 7.c).

4.1. Scene Mesh Acquisition

To annotate the correct grasping position with collision inspection, it is important to have a full mesh of the scene, which contains objects as well as their platform where the

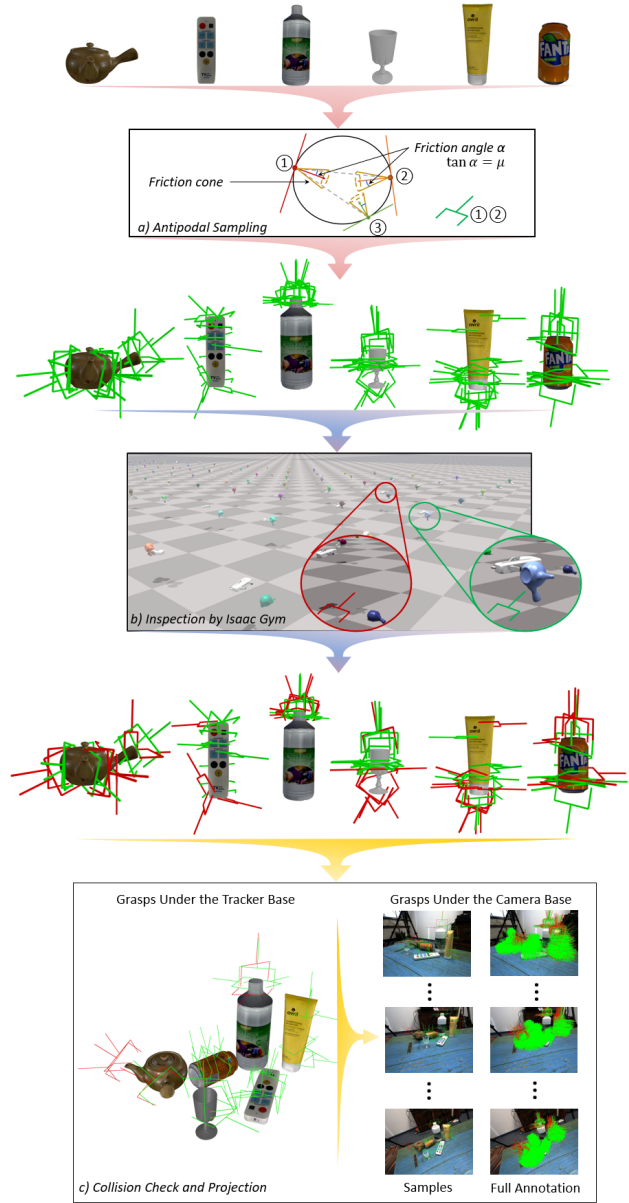


Figure 7. **The pipeline of the grasp annotation process.** We show downsampled grasps for better visualization and show the full annotation at the end for the ultimate performance.

object are placed, such that physical simulation can filter out the grasping points which leads collision of gripper on the other objects and the background. For the objects, we displaced their meshes in the scene with the annotated poses. On the other hand, for the platform, it is not possible to do the same way as the background is not scanned prior. Instead, we reconstruct the scene with the depth images with the corresponding camera poses using truncated signed distance fusion and hole followed by manual hole

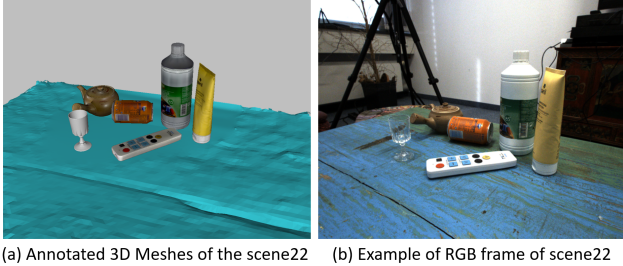


Figure 8. **Example of Mesh Annotation and Its Corresponding RGB Image.** We annotate the scene by reconstructing the platform and displacing the objects’ meshes with their pose. Note that we do not reconstruct the other parts of background such as wall as they are not necessary for grasping simulation.

filling with Artec Studio 17 Professional (Artec3D, Senningerberg, Luxembourg). An example of the 3D mesh of objects with the reconstruction of the platform is shown in Fig. 8 with an example of an RGB frame from the corresponding scene.

4.2. Antipodal Sampling

Antipodal sampling is a wide-used technique for grasp pose generation, which has been investigated in several previous works [4, 8, 12]. Given an object mesh, this scheme first samples an arbitrary point on the mesh surface as the initial contact point (①) together with a line within a range around the surface normal. The sampling threshold $\mu = \tan(\alpha)$ with the friction angle α restricts the range at which rays can be emitted. A second point (② / ③) is found as the intersection of both mesh and line. Then reject sampling is used to prune the point whose line is not inside the friction cone (③) or whose distance from the initial point is beyond the max width of the gripper model. A successfully sampled grasp G_{obj} is then derived by taking the center point between two contact points (①②) and a randomly sampled rotation around the line. Here, in this work, we set μ as 0.4. The end-effector model we use is a Franka Emika parallel-jaw gripper, as shown in Fig. 6.

4.3. Simulation Inspection

After obtaining grasp samples, we use a physical engine, namely Isaac Gym, to inspect grasps which are successful. For each object, we parallelly create the same number of simulation environments as of grasps belonging to the object. We inspect whether these grasps are successful by calculating the distance between the gripper and the centroid of the object model 15 seconds after the finger closure defined by individual grasping width. If the distance is less than $0.1m$, we label this grasp as a successful one and vice versa.

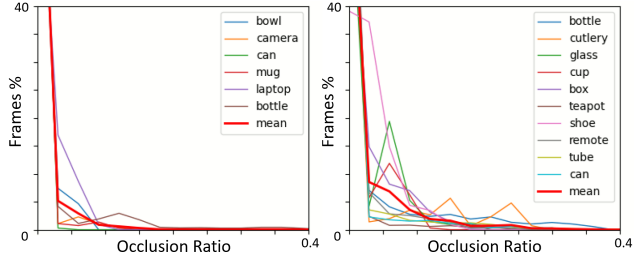


Figure 9. **Occlusion Comparison between NOCS [10] and HouseCat6D.** HouseCat6D covers more occlusions as well as more frequency on the occlusion, which makes the dataset more challenging as well as closer to the real-life scenario.

4.4. Grasp Projection

This is a two-stage procedure. We retrieve objects in each scene and replicate the first-stage projection for all objects in the scene, where we transform the grasps belonging to an object to the tracker base according to the object pose and check their collisions with the surrounding meshes, including other objects and the background. The collision checking module is from the public library Trimesh¹. Then we project all grasps to every image frame to obtain the final dataset, utilizing the camera trajectory recorded under the tracker base.

5. Occlusion Analysis

When it comes to detecting the objects and estimating the pose, occlusion and visibility take important roles. In our dataset, we provide the visibility ratio of each category in the scene per frame. The visibility is calculated as follows. Firstly, we render the mask of an object with a given pose, one object per time to prevent occlusion between categories, and count number of pixels in the mask M_{full}^{cat} . Then masks of categories are rendered again but all together so that occlusion is accounted, followed by counting the number of pixels on each object $M_{occluded}^{cat}$, which now has fewer pixels due to occlusion from other objects. Occlusion ratio is calculated as $M_{occluded}^{cat} / M_{full}^{cat}$, which then averaged over all frames and scenes. We show the ratio on our dataset and as well as on NOCS dataset [10] in Fig. 9 to emphasize the difference in terms of the occlusion in the dataset.

6. Evaluation on Rotation Translation Metric

In Tab. 2, we show the evaluation of baseline on rotation and translation error metric with two sets of thresholds: $10^\circ 5cm$ and $20^\circ 5cm$. Similar to 3D IOU, CenterSnap [6] performs poorly in our dataset. As mentioned in the main

¹<https://trimsh.org/trimesh.collision.html>

Table 1. **Ablation Study on Different Input** Class-wise evaluation of 3D IoU (at 25%/ at 50%) for FS-Net [1] with different training setup.

Approach	Train Set	3D ₂₅ / 3D ₅₀	Bottle	Box	Can	Cup	Remote	Teapot	Cutlery	Glass	Tube	Shoe
FS-Net [1]	RV	66.1 / 29.2	61.8 / 41.0	32.7 / 11.4	99.9 / 62.3	89.2 / 36.0	63.3 / 42.7	58.3 / 42.2	28.2 / 0.8	96.0 / 23.0	75.4 / 11.6	51.7 / 33.3
	RS	60.8 / 21.5	65.9 / 40.8	33.2 / 7.7	100 / 56.0	70.6 / 13.2	56.4 / 36.9	48.4 / 27.3	24.0 / 0.4	94.3 / 3	75.2 / 4.4	44.7 / 30.0
	RV+RS	56.9 / 16.8	63.3 / 37.0	33.6 / 6.7	99.9 / 63.3	68.2 / 6.3	49.0 / 22.4	51.1 / 19.6	24.6 / 0.5	90.9 / 9.7	75.7 / 5.2	37.8 / 17.2
	Full	69.4 / 37.0	64.0 / 42.7	29.4 / 12.7	99.6 / 75.1	92.3 / 54.1	62.6 / 45.3	69.1 / 54.2	43.5 / 10.6	97.2 / 28.2	72.2 / 14.9	58.2 / 38.2
	GT Depth	80.4 / 57.6	66.4 / 45.3	35.9 / 7.5	99.9 / 99.8	100.0 / 99.8	60.3 / 39.6	98.3 / 74.4	41.5 / 21.4	100.0 / 59.5	91.7 / 28.6	95.9 / 87.7

Table 2. **Quantitative Evaluation on Rotation and Translation Metric.** For rotation and translation metric, we show average accuracy over all categories.

Threshold	CenterSnap [6]	GPV-Pose [3]	FS-Net [1]
10°5cm	1.3	8.8	7.3
20°5cm	2.2	23.8	23.0

paper, we suspect this is due to the one-shot training approach in CenterSnap [6], in which the detection part is not pre-trained with larger detection dataset which eventually has an issue with generalization on test sets that have different backgrounds and objects. On the other hand, geometric guided approach such as GPV-Pose [3] and FS-Net [2] has better performance with ground truth detection mask, but compared to 3D IOU metric, performance on GPV-Pose [3] is slightly higher than FS-Net [2].

7. Ablation Study

We trained FS-Net [1] on our dataset with different setups, such as reduced viewpoint coverage of camera (RV), reduced number of scenes (fewer objects per category) (RS), both combined (RV+RS) and higher quality depth (GT Depth) input, to study the impact of different aspect of the dataset on category level 6d pose estimation task. For RV and RS setup, we specifically mimic the coverage of PhoCal [11] by using less number of scenes (RS) and selecting the subset of camera trajectory as continuous 250 frames of translation-dominated motion (RV). For RV+RS, we applied both aspects to mimic the exact setup of PhoCal [11].

Impact of View VS Scenes Compared to having reduced viewpoints (RV), reducing the scene (RS) has a more negative impact on the test scene. As the main task of category-level pose estimation is about generalizing on the unseen objects of known categories, we find it beneficial to see more objects and backgrounds even if the viewpoint is limited. This further stressed the advantage of our dataset over NOCS dataset [10] and PhoCal dataset [11] for both the number of scenes and the number of objects. Furthermore, when both RS and RV are combined, there is a significant drop in the performance, which gives an advantage of our dataset over PhoCal [11], where the robotic arm annotations have a clear limitation on the viewpoint coverage as well as the number of scenes.

Impact of Depth on Geometry Guided Approach Ablation study with GT depth is shown in Tab. 1, GT Depth row. As the geometric-guided approach directly uses the point cloud from the depth map, using GT depth gives a huge boost. However, there was a trivial boost in some categories, such as Bottle, Box, Remote, Cutlery, and Tube. For the box category, we find that with just one view is often hard to judge the dimension of the box and predict the correct orientation, which results in lower 3D intersections. On the other hand, we observed that the performance boost also depends on the diversity of the location an object appears in the dataset. Some categories are more randomly placed (*e.g.* Bottle, Remote Cutlery, and Tube) and have less performance boost compared to more commonly placed categories (*e.g.* cup, teapot, and glass are always standing). For example, the former objects are lying on the side of tables, leaning on the other objects. This makes the prediction challenging. Such behavior indicates that existing methods rely on the regularity of data and hence enlarge the difference between a dataset and the real-world scenario. With the number of scenes under various setups in our dataset, we believe that it can help narrow the domain gap.

References

- [1] Wei Chen, Xi Jia, Hyung Jin Chang, Jinming Duan, Linlin Shen, and Ales Leonardis. Fs-net: Fast shape-based network for category-level 6d object pose estimation with decoupled rotation mechanism. In *Proceedings of the IEEE/CVF Conference on Computer Vision and Pattern Recognition (CVPR)*, pages 1581–1590, June 2021. 6
- [2] Wei Chen, Xi Jia, Hyung Jin Chang, Jinming Duan, Linlin Shen, and Ales Leonardis. Fs-net: Fast shape-based network for category-level 6d object pose estimation with decoupled rotation mechanism. In *Proceedings of the IEEE/CVF Conference on Computer Vision and Pattern Recognition*, pages 1581–1590, 2021. 6
- [3] Yan Di, Ruida Zhang, Zhiqiang Lou, Fabian Manhardt, Xi-angyang Ji, Nassir Navab, and Federico Tombari. Gpv-pose: Category-level object pose estimation via geometry-guided point-wise voting. In *Proceedings of the IEEE/CVF Conference on Computer Vision and Pattern Recognition*, pages 6781–6791, 2022. 6
- [4] Clemens Eppner, Arsalan Mousavian, and Dieter Fox. Acronym: A large-scale grasp dataset based on simulation. In *2021 IEEE International Conference on Robotics and Automation (ICRA)*, pages 6222–6227. IEEE, 2021. 5
- [5] Berthold Horn, Hugh Hilden, and Shahriar Negahdaripour. Closed-form solution of absolute orientation using orthonormal matrices. *Journal of the Optical Society of America A*, 5:1127–1135, 07 1988. 3
- [6] Muhammad Zubair Irshad, Thomas Kollar, Michael Laskey, Kevin Stone, and Zsolt Kira. Centersnap: Single-shot multi-object 3d shape reconstruction and categorical 6d pose and size estimation. In *2022 International Conference on Robotics and Automation (ICRA)*, pages 10632–10640, 2022. 5, 6
- [7] HyunJun Jung, Patrick Ruhkamp, Guangyao Zhai, Nikolas Brasch, Yitong Li, Yannick Verdie, Jifei Song, Yiren Zhou, Anil Armagan, Slobodan Ilic, Ales Leonardis, and Benjamin Busam. Is my depth ground-truth good enough? hammer – highly accurate multi-modal dataset for dense 3d scene regression, 2022. 3
- [8] Jeffrey Mahler, Jacky Liang, Sherdil Niyaz, Michael Laskey, Richard Doan, Xinyu Liu, Juan Aparicio Ojea, and Ken Goldberg. Dex-net 2.0: Deep learning to plan robust grasps with synthetic point clouds and analytic grasp metrics. In *Robotics: Science and Systems (RSS)*, 2017. 5
- [9] Viktor Makoviychuk, Lukasz Wawrzyniak, Yunrong Guo, Michelle Lu, Kier Storey, Miles Macklin, David Hoeller, Nikita Rudin, Arthur Allshire, Ankur Handa, and Gavriel State. Isaac gym: High performance gpu-based physics simulation for robot learning, 2021. 4
- [10] He Wang, Srinath Sridhar, Jingwei Huang, Julien Valentin, Shuran Song, and Leonidas J Guibas. Normalized object coordinate space for category-level 6d object pose and size estimation. In *Proceedings of the IEEE Conference on Computer Vision and Pattern Recognition*, pages 2642–2651, 2019. 1, 5, 6
- [11] Pengyuan Wang, HyunJun Jung, Yitong Li, Siyuan Shen, Rahul Parthasarathy Srikanth, Lorenzo Garattoni, Sven Meier, Nassir Navab, and Benjamin Busam. Phocal: A multi-modal dataset for category-level object pose estimation with photometrically challenging objects. In *CVPR*, 2022. 6
- [12] Guangyao Zhai, Yu Zheng, Ziwei Xu, Xin Kong, Yong Liu, Benjamin Busam, Yi Ren, Nassir Navab, and Zhengyou Zhang. Da² dataset: Toward dexterity-aware dual-arm grasping. *IEEE Robotics and Automation Letters*, 7(4):8941–8948, 2022. 5